Monthly Notices of the ROYAL ASTRONOMICAL SOCIETY

MNRAS **536,** 3277–3283 (2025) https://doi.org/10.1093/mnras/stae2814
Advance Access publication 2024 December 26

High-resolution studies of the C-band and L-band radio continuum of the periodic methanol maser source G9.62+0.20E and surrounding sources

B. Woode [1,2★] M. G. Hoare [3] A. Kuditcher[2] and S. Goedhart [4]

[1]Ghana Space Science and Technology Institute, Ghana Atomic Energy Commission, P. O. Box LG 80, Legon, Accra, Ghana
[2]Department of Physics, University of Ghana, P.O. Box LG 63, Legon, Accra, Ghana
[3]School of Physics and Astronomy, The University of Leeds, Woodhouse Lane, Leeds LS2 9JT, UK
[4]South African Radio Astronomy Observatory, 2 Fir Street, Observatory, 7925, South Africa

Accepted 2024 December 19. Received 2024 December 19; in original form 2023 June 12

ABSTRACT

High-resolution observations of the *C*-band and *L*-band radio continuum of the hypercompact H II region G9.62+0.20E conducted with the e-MERLIN interferometric array are presented. A flux density of 2.25 ± 0.20 mJy and an angular size of 127 ± 22 mas were measured for the *C*-band continuum. At *L* band, an upper limit of 162 μJy on the integrated flux density was calculated at the continuum's position. The surrounding sources C and D were detected at levels consistent with previous detections. The results for source E requires a steeper spectrum at *L* band than previous observations extrapolated from higher frequencies. This can be explained with a truncated inverse square law density distribution model. We obtain a *C*-band peak brightness temperature of about 4000 K, which assuming an electron temperature of 10^4K translates to an optical depth of 0.5, indicating the continuum is optically thin at *C* band going thick at *L* band. These results therefore place firm constraints on H II region models in source E. The periodic variability of methanol masers, as seen in G9.62+0.20E, has been explained with the pulsating star, accretion disc, and colliding wind binary models. Some models predict a hypercompact H II region can provide pumping for methanol masers. In the colliding wind binary model context maser variability is attributed to seed photon modulation. Hence, future H II models matching our observations could test predictions of these models in terms of the variability profiles of the 1.6 GHzOH and 6.7 GHz methanol masers.

Key words: masers – stars: formation – stars: massive – (ISM:) H II regions – radio continuum: stars.

1 INTRODUCTION

The 6.7 GHz methanol transition in G9.62+0.20E was reported to show periodic changes in its flux density in the form of regular flares with a period of 244 d (Goedhart, Gaylard & van der Walt 2003, 2004). Ten years of further monitoring of the regularly varying source using the Hartebeesthoek 26 m telescope produced more results to confirm this periodic variation (Goedhart et al. 2014). Closely associated with methanol masers in newly formed massive stars in massive star-forming regions are hydroxyl masers. The spatial coexistence of the two species was revealed observationally by interferometric observations (Caswell, Vaile & Forster 1995). This is supported by modelling the conditions necessary for maser formation, which show that both OH and methanol masers are likely pumped by infrared dust emission (Cragg, Sobolev & Godfrey 2002). A recent monitoring exercise of the 1667 MHz OH masers by Goedhart et al. (2019) revealed flare profiles similar to the methanol masers but with pronounced dips. This has been explained by Goedhart et al. (2019) to be a result of the electron temperature of the ionized outer section of the H II region being increased by photons with energy in excess of 100 eV.

The source of the flares in these maser's intensity has been interpreted in a number of ways with several models. These are the pulsating star model, (Inayoshi et al. 2013; Sanna et al. 2015), accretion disc model (Araya et al. 2010; Parfenov & Sobolev 2014), and the colliding wind binary model (van der Walt, Goedhart & Gaylard 2009). In these models, the explanations for the periodicity are given by either invoking the presence of a binary system (der Walt et al. 2009; Araya et al. 2010; Parfenov & Sobolev 2014) or a pulsating star (Inayoshi et al. 2013; Sanna et al. 2015). The binary system model include two accretion disc models (Araya et al. 2010; Parfenov & Sobolev 2014) and the colliding wind binary model (CWB) (der Walt et al. 2009). Several methanol maser models have also invoked the presence of an H II region. Sobolev & Deguchi (1994a, b) used a background H II region to provide the seed photons for maser models that are pumped by dust emission. However, Slysh, Kalenskii & Val'tts (2002) and Sobolev et al. (2007) used the free–free emission from a hypercompact H II region of high emission measure to actually provide the pumping for the methanol masers instead.

In the colliding wind binary model employed to explain the observed periodic variabilities of such masers (der Walt et al. 2009; van der Walt 2011a, b; van den Heever et al. 2019) it is the variations in the seed photons from a background H II region, which are periodically modulated that cause the observed periodicity.

★ E-mail: Benedictawoode25@gmail.com

Additional ionizing photon flux is produced in the hot post-shock gas when the stellar winds of the young binary stars powering the H II region collide at periastron. This can have an effect on the H II region in terms of the change in the free–free emission. The masers projected against the H II region amplify this change and respond with a flare. In the colliding wind binary model, the masers are still pumped by infrared emission from the hot dust associated with the H II region. If the masers were instead pumped by the free–free emission from a hypercompact H II region as proposed by Slysh et al. (2002) and Sobolev et al. (2007) any variations in the H II region could also result in maser variability.

The accretion disc models employ the accretion of materials on to the disc of a protostar to explain the dust temperature variation which is assumed to cause the periodic variability of the maser. Accretion events in massive young stellar objects have resulted in an increase in the radio continuum emission from the ionized jets present as observed by Cesaroni et al. (2018, 2023) and Obonyo et al. (2021), which are accompanied by a flare in the methanol masers (Fujisawa et al. 2015). The accretion event in G323.46−0.08 also resulted in a methanol maser flare (Proven-Adzri et al. 2019) with modelling by Wolf et al. (2024) showing that the maser behaviour was actually consistent with an increase in pumping by the associated increase in the infrared emission from dust.

In another accretion disc model, the observed variabilities in formaldehyde and methanol masers are explained as due to periodic accretion of material from a circumbinary disc in a young eccentric binary system that heats the dust and changes the pumping radiation field (Araya et al. 2010). Here, the material from the circumbinary disc is accreted on to the individual protostar, heating the dust and increasing the infrared radiation field resulting in the large maser gain which leads to the high amplification. This model follows predictions of the smoothed particle hydrodynamics simulations (Artymowicz & Stephen 1996) to arrive at this results. Parfenov & Sobolev (2014), however, proposes periodic emission from rotating spiral shocks in the central gap of a circumbinary accretion disc around young binary stars to heat up the dust. The variation in dust temperature is caused by radiation from the bow shock illuminating the dust which may again change the infrared pumping field.

For the pulsating star model derived from the swollen star model, a growing protostar under rapid mass accretion rate $\dot{M}_* \gtrsim 10^{-3}\,\mathrm{M}_\odot\,\mathrm{yr}^{-1}$ may pulsate upon becoming unstable before reaching the Zero Age Main Sequence (ZAMS) (Hosokawa & Omukai 2009; Hosokawa, Yorke & Omukai 2010). Inayoshi et al. (2013) invoked the pulsational instability of a bloated protostar with a high-accretion rate to explain the observed maser periodicity and predicted that the period depends on the adopted accretion rate and gets longer with increasing accretion rates. In the pulsating star model, the modulation of the infrared pumping radiation associated with the massive star results in the periodicity of the masers. Sanna et al. (2015) also invoked the presence of an independent pulsating massive young protostar with high-accretion rate of $4 \times 10^{-3}\,\mathrm{M}_\odot\,\mathrm{yr}^{-1}$ (Liu et al. 2011) and the superposition of two independent infrared radiation fields to explain the variable maser behaviour in G9.62+0.20E. The colliding wind binary model in G9.62+0.20E requires the presence of an H II region. Hence, studies of its radio continuum emissions are particularly relevant. Previous Very Long Array (VLA) and Very Long Baseline Array (VLBA) radio continuum astrometry has been used to show the positions of masers relative to the 43 GHz UCH II region in G9.62+0.20E (Sanna et al. 2015).The results of the VLA continuum (UCH II) at 43 GHz however, does not map the actual seed photons in the continuum at 1.6 and 6.7 GHz and that is addressed by this paper.

Table 1. Observing parameters at *L* band.

Parameter	*L* band
Project code	CY5204_L
Obs. dates (06_2017)	16,17,18,19
Number of sources	6
Time on source (h)	10.32
Integration time (s)	1.0
Flux cal (1331+305) (Jy)	13.8 ± 0.2
Bandpass cal (1407+284) (Jy)	1.013 ± 0.003
Phase cal (1751−1950) (Jy)	0.057 ± 0.002
Frequency range (GHz)	1.25–1.76
Spectral windows	8
Spectral window bandwidth (MHz)	64
Channel width (MHz)	0.5
Channels per spectral window	128
Total bandwidth (MHz)	512
Polarization	RR, RL, LR, LL

Table 2. Observing parameters at *C* band.

Parameter	*C* band
Project code	CY5204_C
Obs. dates (07_2017)	11,14,16,17
Number of sources	5
Time on source (h)	20.18
Integration time (s)	1.0
Flux cal (1331+305) (Jy)	6.5 ± 0.1
Bandpass cal (1407+284) (Jy)	1.51 ± 0.01
Phase cal (1751−1950) (Jy)	0.0832 ± 0.0003
Frequency range (GHz)	6.300–6.812
Spectral windows	4
Spectral window bandwidth (MHz)	128
Channel width (MHz)	1
Channels per spectral window	128
Total bandwidth (MHz)	512
Polarization	RR, RL, LR, LL

2 OBSERVATIONS AND DATA REDUCTION

2.1 Observations

The e-MERLIN interferometric array was used for the observation of both the L-band and the C-band radio-continuum. The OH and the methanol masers were also observed but due to astrometry accuracy issues the results are not reported in this paper. During the observations each observing run consisted of 60 min on the flux calibrator (1331+305), 60 min on the bandpass calibrator (1407+284), and sequences of 3 min on the phase calibrator (1751−1950) and 7 min on the source (science target) (1806−2301) which were repeated for the total on-source duration, and finally 60 min on the polarization calibrator (0319+415). For the observations at *L* band 10.32 h were spent on the source. The data were taken in full polarization over a frequency range of 1.25−1.76 GHz with a total bandwidth of 512 MHz which was divided into eight adjacent spectral windows each having 64 channels. Table 1 summarizes the observing parameters used for the continuum data collection. Due to low elevation of the target the data were built up over 4 d.

At C-band 20.18 h were spent on the source. The data were taken in full polarization over a frequency range of 6.3–6.8 GHz with a total bandwidth of 512 MHz which was divided into four adjacent spectral windows each having 128 channels. Table 2 gives the parameters used for the acquisition of the data. Due to low elevation of the target the data were again built up over 4 d.

Tables 1 and 2 also contain the observed calibrators and their scaled flux densities at L and C-band, respectively. The flux calibrator was used as a primary calibrator and the phase calibrator, bandpass calibrator, and polarization calibrator were used as secondary calibrators.

2.2 Data reduction

The data were reduced with the e-MERLIN Common Astronomy Software Applications (CASA) pipeline version v0.10.02. The pipeline was run twice on the data set first for pre-processing which involved flagging bad data, and then subsequently applying standard calibration techniques. For the calibration, 3C286 (1331+305) was first used to calibrate the flux density of the other calibrator sources. Then source 1751−1950 was used for the phase calibration and source 1407+284 for the bandpass calibration.

Further data processing, imaging, and analysis were carried out with the CASA (version 5.4.2–1) and IPYTHON (version 5.1.0) packages using standard procedures. The initial calibration revealed a weak phase calibrator source hence, self-calibration was used to obtain better images.

At L band the model of G9.745+0.106, a source within the field of view of G9.62+0.20E which has an integrated flux density of 91.5 mJy was used for the self calibration. This source has been previously observed with the VLA to have an integrated flux density of 198 mJy at L band (Becker et al. 1994). For the *C*-band data set the model of the brightest maser line was used for the self-calibration. The Stokes I continuum map of the area of the known OH and methanol maser emission was made by making a multifrequency synthesis image of the four spectral windows excluding the maser line channel. A Gaussian fit on the emission yielded parameters which gave estimates of properties such as the flux density, position angles, and full width at half-maximum.

3 RESULTS

3.1 G9.62+0.20E

3.1.1 The C-band continuum

Fig. 1 shows the image of the *C*-band continuum with its flux density and size parameters given in Table 3. A flux density of 2.25 ± 0.20 mJy was measured from the free–free emission of the continuum. The position however is offset by 320 mas in RA and 152 mas in Dec. when compared with the *Q*-band Jansky Very Long Array (JVLA-A) position in table 1 of (Sanna et al. 2015) due to poor astrometric accuracy of the e-MERLIN observations. We measured the rms noise to be 50 μJy beam^{-1}. For a 20 h continuum observation at this frequency under good conditions a theoretical rms noise limit of 8 μJy beam^{-1} is expected. A number of reasons such as low elevation of the source and bad weather conditions are thought to be the cause of this high noise.

The geometric mean of the *C* band major and minor deconvolved sizes is 127 ± 22 mas when extrapolated from the source sizes in Table 3.

This corresponds to a physical size of 0.0032 pc at the 5.2 kpc distance of G9.62+0.20E (Sanna et al. 2015). This places the source in the hypercompact category in the Kurtz–Franco classification system (Kurtz & Franco 2002). The measured VLA *Q* band size of 81 ± 5 mas for this source (Sanna et al. 2015) in Table 4 translates to a physical size of 0.0020 pc. From the results presented in this work, the source size is comparable but larger than the *Q* band size suggesting the source size is getting larger at low frequencies. In terms of a power-law dependence of size on frequency the slope is -0.24 ± -0.09. This behaviour is characteristic of sources with a steeply falling density gradient (Panagia & Felli 1975).

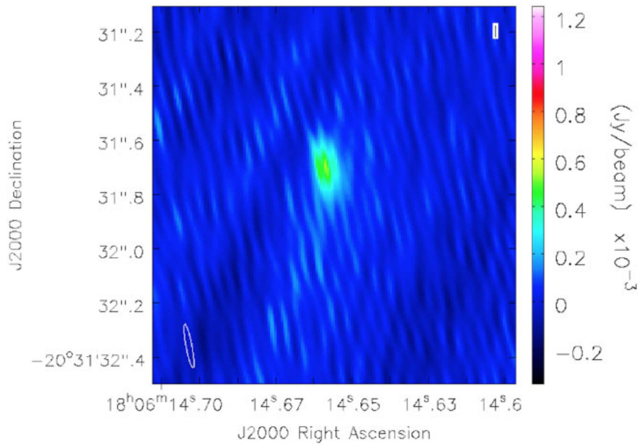

Figure 1. Image of the *C*-band radio continuum of G9.62+0.20E. At the lower left corner of the image is the synthesized beam of size 0.16 arcsec × 0.02 arcsec at a position angle of 10.55 °.

3.1.2 The L-band continuum

Fig. 2 shows the site for the G9.62+0.20E star-forming region at L band with the expected position of the continuum emission marked with a pink cross. At this position no radio continuum emission was recorded above the e-MERLIN sensitivity limit. An rms noise value of 54 μJy beam^{-1} was measured which is a 1σ limit on the peak flux. At L band with a target well above an elevation of 20°, under good conditions and with vigorous radio frequency interference (RFI) removal techniques a theoretical noise limit of 14 μJy beam^{-1} is expected for a 12 h continuum observation for e-MERLIN without Lovell. The 54 μJy beam^{-1} noise level which is almost four times the expected value is likely due to the low elevation, bad weather conditions, side lobes from nearby sources G9.62+0.20C, G9.62+0.20D, and also contributions from source G9.62+0.20A and G9.62+0.20B (Garay et al. 1993). The loss of the long north–south most sensitive Cambridge baseline gives a larger beam size which also resulted in the increase in the noise. The upper limit on the flux density was obtained by finding the average of the absolute values of the flux from five boxes taken around the pink cross. This resulted in a value of 54 μJy which gives a 3σ upper limit on the flux density of 162 μJy. The spectral energy dictribution (SED) plot of the flux density for G9.62+0.20E has been plotted in fig. 5 of Franco et al. (2000) with frequencies 8.6, 14.97, 22.23, 43.34, and 110 GHz. A spectral index of 0.95 ± 0.06 was calculated for this region (Franco et al. 2000). Fig. 3 shows the updated SED plot with our *C*-band flux density and the upper limit on the *L*-band continuum added. Our *L* band upper limit is significantly lower than the expected flux of 600 μJy, which comes from extrapolating the higher frequency measurements from Franco et al. (2000) using their spectral index of 0.95.

In the figure the results for the 230 GHz continuum flux density from Liu et al. (2017) is added. The fit to these results yield a spectral index of 1.28 ± 0.03.

Table 3. Flux density of the *C*-band continuum of G9.62+0.20E and G9.62+0.20D. Also given are the deconvolved sizes and the position angles (PA).

Source	Integrated flux (mJy)	Peak flux (mJy beam^{-1})	Deconvolved size $\Theta_{\mathrm{maj.}}$(mas) $\times$ $\Theta_{\mathrm{min.}}$(mas)	PA (°)
G9.62+0.20E	2.25 ± 0.20	0.520 ± 0.001	$165 \pm 42 \times 97 \pm 23$	176 ± 28
G9.62+0.20D	43.4 ± 2.0	1.24 ± 0.02	$734 \pm 19 \times 541 \pm 16$	58.9 ± 3.9

Table 4. The sizes of G9.62+0.20E as measured by fitting a Gaussian using *imfit* routine at both *C* and *Q* band. The size of the *Q*-band continuum comes from Sanna (private email communication) based on the results in Sanna et al. (2015).

Band	Beam size (mas)	PA (°)	Observed size $\Theta_{\mathrm{maj.}}$(mas) $\times$ $\Theta_{\mathrm{min.}}$(mas)	PA (°)	Deconvolved size $\Theta_{\mathrm{maj.}}$(mas) $\times$ $\Theta_{\mathrm{min.}}$(mas)	PA (°)
Q	93×50	-1.5	$145 \pm 5 \times 77 \pm 3$	174 ± 2	$112 \pm 7 \times 58 \pm 6$	172 ± 6
C	160×20	10.55	$229 \pm 26 \times 102 \pm 9$	5 ± 2	$165 \pm 42 \times 97 \pm 23$	176 ± 28

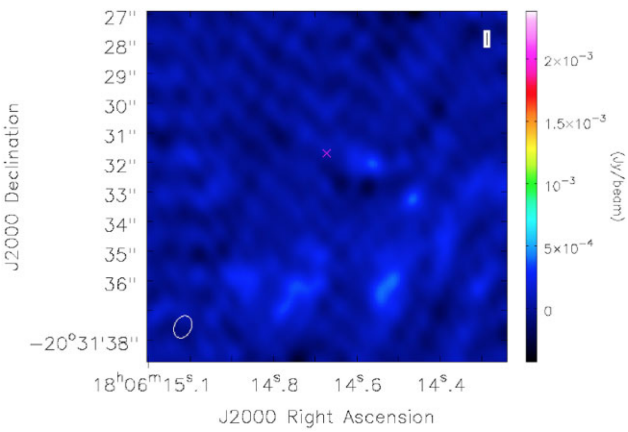

Figure 2. Image of the field of the *L*-band radio continuum of G9.62+0.20E. The cross shows the expected position of the radio continuum. Shown at the lower left corner of the image is the synthesized beam of size 0.78 arcsec × 0.57 arcsec at a position angle of $-25.36°$.

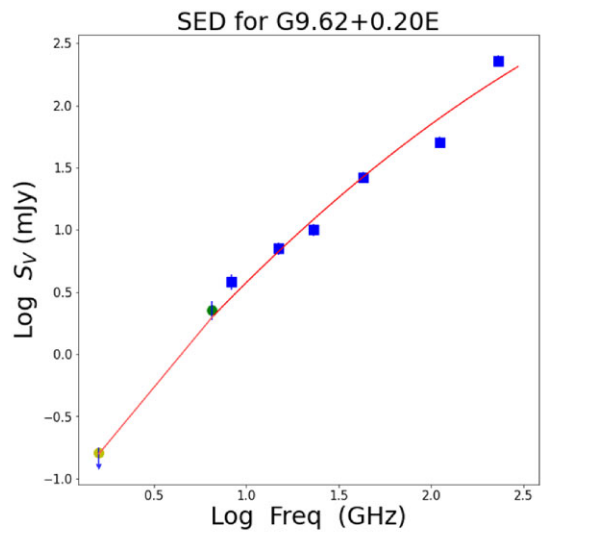

Figure 3. An updated spectral index plot of the continuum flux density distribution of the G9.62+0.20E region at 8.6, 14.97, 22.23, 43.34, and 110 GHz adapted from Franco et al. (2000) and the continuum flux density at 230 GHz from Liu et al. (2017). The update to the plot is the flux density for the *C*-band continuum shown with a circle and the 3σ upper limit of the peak flux density at *L* band also shown with a circle. The solid line represents the theoretical spectrum for an inverse square distribution of ionized gas at 10^4 K truncated at some finite outer radius of $r_{\mathrm{out}} = 0.0014$ pc.

3.2 G9.62+0.20C

3.2.1 The L-band continuum

At *L* band, we also detected the UCH II region G9.62+0.20C (Garay et al. 1993) as seen in Fig. 4. Table 5 gives the position and the flux density of G9.62+0.20C. The continuum morphology of the *L*-band emission from G9.62+0.20C is consistent with the cometary morphology seen at 8.6 GHz in Kurtz et al. (1994) with the tail emission breaking up at the e-MERLIN resolution. The size of the structure however cannot be determined by Gaussian fit, hence an estimate of 3 arcsec is made by inspection. The measured flux density of 22.1 ± 1.9 mJy compares favourably with the flux density of 26 mJy at 1.4 GHz measured by Becker et al. (1994). A previous observation by Kurtz et al. (1994) at 8.6 GHz measured a flux density of 175 mJy whereas at 4.9 GHz Garay et al. (1993) measured 50 mJy.

Note that at *C*-band continuum emission from G9.62+0.20C was completely resolved out and not detected.

The SED plot for G9.62+0.20C is shown in Fig. 5 with flux densities at 4.9, 8.6, 15, 15, and 23 GHz adapted from Garay et al. (1993), Kurtz et al. (1994), and Cesaroni et al. (1994), respectively. Note that there is considerable disagreement between the flux densities for this source in literature as clearly demonstrated in

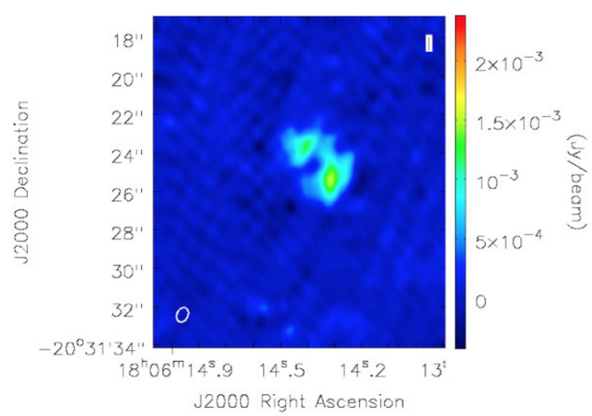

Figure 4. Image of the *L*-band radio continuum emission of G9.62+0.20C. At the lower left corner of the image is the synthesized beam of size 0.78 arcsec × 0.57 arcsec at a position angle of $-25.36°$.

Table 5. Positions and flux densities of the *L*-band continuum associated with G9.62+0.20C and G9.62+0.20D.

Source	α (J2000)(h m s)	Error (arcsec)	δ (J2000)(° ′ ″)	Error (arcsec)	Integrated flux (mJy)	Peak flux (mJy beam^{-1})	rms (μJy beam^{-1})
G9.62+0.20C	18 : 06 : 14.3522	0.010	−20 : 31 : 24.652	0.013	22.1 ± 1.9	1.50 ± 0.09	52
G9.62+0.20D	18 : 06 : 14.9514	0.011	−20 : 31 : 42.620	0.045	11.8 ± 0.5	2.38 ± 0.10	52

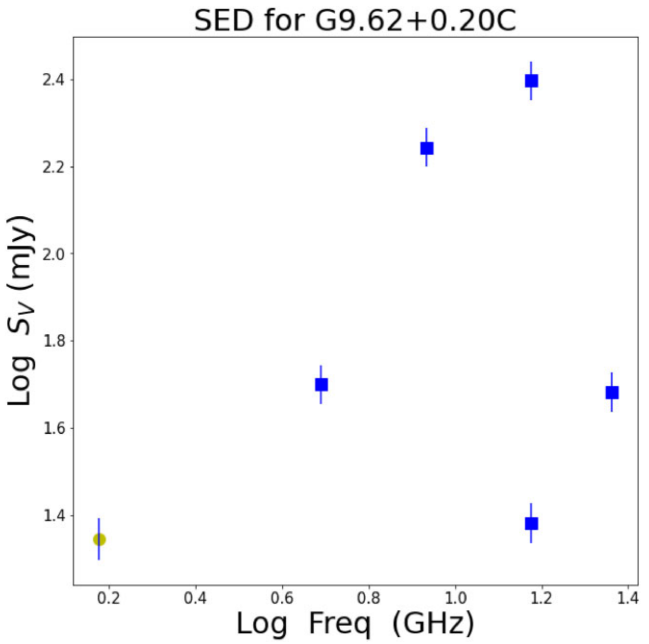

Figure 5. A spectral index plot of the continuum flux density distribution of the G9.62+0.20C region at 4.9, 8.6, 15, 15 , and 23 GHz adapted from Garay et al. (1993), Kurtz, Churchwell & Wood (1994), and Cesaroni et al. (1994), respectively. The update to the plot is the flux density for the *L*-band continuum shown with a yellow circle.

Fig. 5, this could be as a result of different structures being resolved since it is an extended region with a lot of structure.

3.3 G9.62+0.20D

3.3.1 The C-band continuum

In the field of view of the C-band continuum for G9.62+0.20E is the source G9.62+0.20D shown in Fig. 6. Presented in Tables 3 and 5 are the position, flux density, and sizes for the source G9.62+0.20D. At 6.5 GHz the H II region is cometary in shape and has a flux density of 43 mJy. A flux density of 70 mJy at 4.9 GHz had been reported previously by Garay et al. (1993), whilst Becker et al. (1994) report a flux density of 36.6 mJy at 5 GHz. A flux of 65.8 mJy was measured at 8.6 GHz by Kurtz et al. (1994). The recorded flux in comparison with the expected flux suggests most of the flux being recovered. The cometary morphology is also consistent with the 8.6 GHz radio continuum image in Testi et al. (2000).

3.3.2 The L-band continuum

The radio continuum emission at *L* band from G9.62+0.20D is shown in Fig. 7. Table 5 presents the positions and flux density of the source. At *L* band a flux density of 11.84 ± 0.5 mJy was recorded for the source. At 1.4 GHz an upper limit of 17 mJy is reported by Becker et al. (1994), but inspection of the cut out images indicates a source with a flux of 10 mJy which is consistent with the recorded flux of 11.8 mJy.

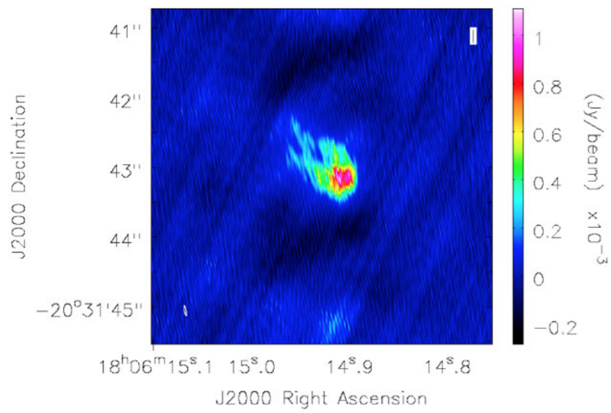

Figure 6. *C*-band radio continuum image of G9.62+0.20D. At the lower left corner of the image is the synthesized beam.

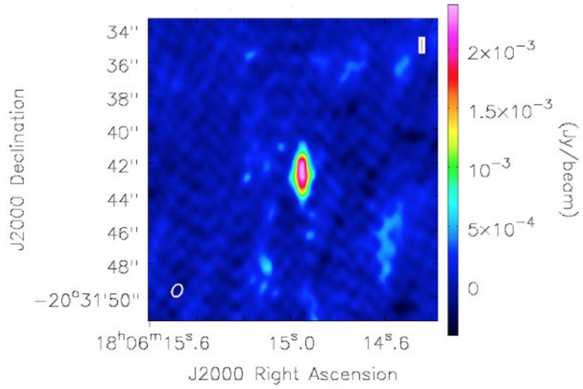

Figure 7. Image of the *L*-band radio continuum emission of G9.62+0.20D with a deconvolved size of (2.090 ± 0.106) arcsec × (0.781 ± 0.025) arcsec and a position angle of (1.9 ± 1.4) degree. At the lower left corner of the image is the synthesized beam of size 0.78 arcsec × 0.57 arcsec at a position angle of −25.36 °.

Fig. 8 shows the SED plot for G9.62+0.20D with flux densities at frequencies of 4.9, 5.0, 8.6, 15, and 23 GHz adapted from Becker et al. (1994), Cesaroni et al. (1994), and Kurtz et al. (1994) respectively. The flux densities at these frequencies produced a spectral index of 0.81 ± 0.05.

4 DISCUSSION

The H II region associated with G9.62+0.20E has been detected at 6.5 GHz. This is the first *C*-band continuum detection of this source. The shape of the H II region is elliptical and agrees with a similar elliptical shape and orientation found by Sanna et al. (2015) at 43 GHz as can be seen from Fig. 1. This work also forms the first

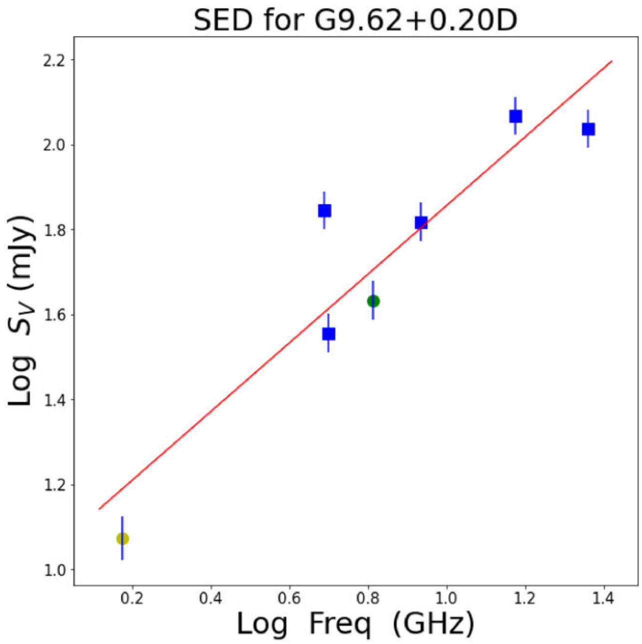

Figure 8. A spectral index plot of the flux density distribution of the G9.62+0.20D region is shown. The flux density at 4.9, 5.0, 8.6, 15, and 23 GHz are adapted from Becker et al. (1994), Cesaroni et al. (1994), and Kurtz et al. (1994), respectively. The solid line is the best fit to the measured flux densities which yields a spectral index of 0.81 ± 0.05 at the peak position. The flux density for our the *C*-band continuum and *L* band are shown with a circle.

L-band continuum study for the G9.62+0.20E massive star-forming region placing an upper limit of 162 µJy on the expected continuum flux density. The non-detection could be attributed to the continuum being too weak to detect or the continuum could be completely resolved out by the interferometer. However, at *L* band the size of the source as extrapolated from *Q* band and *C* band is estimated to be 180 mas which is smaller than our e-MERLIN beam size of about 660 mas. It is therefore likely the measured upper limit of 162 µJy on the flux density is genuine and not an artefact due to resolving out.

Previously, Franco et al. (2000) invoked a steep density gradient ($n \propto r^{-2.5}$) to explain the 0.95 spectral index calculated over the continuum frequency range 8.6 to 110 GHz in G9.62+0.20E. This model predicts that the slope continues to extend to lower frequencies, however with the addition of the *C*-band and *L*-band continuum results and the 230 GHz continuum flux density from Liu et al. (2017) the model no longer explains the low frequency spectrum behaviour.

We adopt the model from Marsh (1975) to explain the behaviour of the SED instead of using the Franco et al. (2000) model. The Marsh model gives an explanation for the behaviour of some radio sources with spectral indices greater than 0.6. Here, an inverse square density distribution of ionized gas which is truncated at some finite radius is assumed for such sources. In the model, the electron density (n) is given by $n = A/r^2$ for $r < r_o$, where r_o is the truncation radius and A is a constant. Following Marsh (1975), we assumed an electron temperature of 10^4 K and computed SEDs for a range of values of A and r_o by solving equations (11) and (12). A truncation radius of 4.6×10^{15} cm and an electron density of 3.9×10^5 cm^{-3} at that radius were calculated resulting in a value of 8.25×10^{36} cm^{-1} for A. This density is similar to those derived by der Walt (2011a) and den Heever et al. (2019) from the maser flare profile under the colliding wind binary model. The truncation radius translates into an angular diameter of 118 mas similar to the deconvolved sizes in Table 4. In comparing the linear fit by Franco et al. (2000) to the power law fit by Marsh (1975) an Lmfit module test was conducted on both. For the linear fit the chi-squared and the reduced chi-squared yielded 67 000 and 9600, respectively. The Akaike Information Criterion (AIC) and the Bayesian Information Criterion (BIC) for the linear fit as well yielded 74.3 and 74.4, respectively. For the power-law fit the chi-squared and the reduced chi-squared yielded 0.6 and 0.1, respectively. The AIC and the BIC in the case of the power law yielded −17.2 and −17.1, respectively. The relatively high values in the chi-square and the reduced chi-square in the linear fit (Franco et al. (2000)) suggests that the model may not be a good fit for the data. The lower AIC and BIC values in the power model (Marsh 1975) indicates that it is a better fitting model data. Thus, the Marsh (1975) model is a better fit of the continuum flux density distribution over the range of frequencies 1.6, 6.5, 8.6, 14.97, 22.23, 43.34, and 110 GHz for the G9.62+0.20E region.

As discussed by Marsh (1975) the turnover of the radio spectrum at low frequencies in G9.62+0.20E can be explained with this model. The turn over in the radio SED indicates that the source is going optically thick. This has been checked by examining the brightness temperature as a function of frequency assuming an electron temperature of 10^4K to estimate the optical depths. We note that the observed electron temperature of an H II region can vary from about 8000 K to 15000 K (Guzman et al. 2012). However, this does not affect the conclusions below. The peak flux at *Q* band corresponds to a peak brightness temperature of about 80 K translating to an optical depth of 0.008. The *C*-band peak flux corresponds to a peak brightness temperature of about 4000 K which translates to an optical depth of 0.5. These optical depth values show that at higher frequencies the source is optically thin and remains marginally optically thin at *C* band. However, when the optical depth is extrapolated to *L* band with the usual $\nu^{-2.1}$ dependence the optical depth will be around 13 and it will be very optically thick.

5 CONCLUSION

A high-resolution map of the *C*-band radio continuum and the upper limit measurement of the *L*-band radio continuum conducted with the e-MERLIN interferometric array of the periodic methanol maser source G9.62+0.20E are reported. These are the lowest frequency studies of this source to date and the extended radio SED puts constraints on the density distribution. A linear fit to the radio SED is no longer a good description. Instead a good fit is obtained using a model with a truncated r^{-2} power-law density distribution. The larger angular size of 127 ± 22 mas measured at *C* band compared to 81 ± 5 mas at *Q* band is also consistent with a falling density distribution.

The colliding wind binary model for periodic masers requires the variation of the seed photons from an H II region to causes the flaring rather than variations in the pumping photons from infrared (IR) emission. High-resolution maps at the actual frequencies of the seed continuum photons of the 1.6 GHzOH masers and 6.7 GHz methanol masers are therefore important to test the colliding wind binary model. The r^{-2} density distribution found from our observations is likely to help explain the relative spatial location of the masers and the variable background continuum. In the modelling by den Heever et al. (2019), a constant density H II region was used and it was found that the outer edge of the H II region only varied by a very small amount. This would require the flaring maser spots to be in a very particular location. However, with a steeply falling density gradient the region where the radio continuum varies significantly is likely to be much larger, alleviating the spatial fine tuning problem.

These new observations will help us to understand the correlated variability of the 1.6 GHzOH mainline masers and the 6.7 GHz methanol maser in G9.62+0.20E. The fact that the free–free continuum emission is optically thin at the methanol maser frequency and optically thick at the OH maser frequency may be relevant for explaining the time delays and dips observed in the 1.6 GHzOH maser (Goedhart et al. 2019). Further attempts to simultaneously map the background seed continuum emission and the position of the variable masers spots are still needed to test these ideas, but this is likely to require the combination of the sensitivity and resolution of Square Kilometer Array (SKA) mid for the southerly G9.62+0.20E source.

ACKNOWLEDGEMENTS

Research reported in this work was supported by a Newton Fund project, Development in Africa with Radio Astronomy (DARA), and awarded by the UK's Science and Technology Facilities Council (STFC) – grant reference ST/R001103/1. We are grateful to Prof. Yaa Ntiamoah Baidoo and the Carnegie Corporation, New York, for part funding this work under the Next Generation of Academics in Africa grants. We are also indebted to the European Union Horizon 2020 Research and Innovation programme via Jumping Jive for funding the data analysis aspect of this work.

DATA AVAILABILITY

The data underlying this article will be shared on reasonable request to the corresponding author.

REFERENCES

Araya E. D., Hofner P., Goss W. M., Kurtz S., Richards A. M. S., Linz H., Olmi L., Sewitlo M., 2010, ApJ, 717, L133
Artymowicz P., Stephen H. L., 1996, ApJ, 467, L77
Becker R. H., White L. R., Helfand D., Zoonematkermani S., 1994, ApJS, 91, 347
Caswell J., Vaile R., Forster J., 1995, MNRAS, 277, 210
Cesaroni R., Churchwell E., Hofner P., Walmsley C. M., Kurtz S., 1994, A&A, 903, 920
Cesaroni R. et al., 2018, A&A, 612, A103
Cesaroni R. et al., 2023, A&A, 680, A110
Cragg D., Sobolev A. M., Godfrey P., 2002, MNRAS, 331, 521
Franco J., Kurtz S., Hofner P., Testi L., Garcia-Segura G., Martos M., 2000, ApJ, 542, L143
Fujisawa K., Yonekura Y., Sugiyama K., Horiuchi H., Hayashi T., Hachisuka K., Matsumoto N., Niinuma K., 2015, Astron. Telegram, 8286, 1
Garay G., Rodriguez L. F., Moran J. M., Churchwell E., 1993, ApJ, 418, 368
Goedhart S., Gaylard M. J., van der Walt D. J., 2003, MNRAS, 339, L33
Goedhart S., Gaylard M. J., van der Walt D. J., 2004, MNRAS, 355, 553
Goedhart S., Maswanganye J. P., Gaylard M. J., van der Walt D. J., 2014, MNRAS, 437, 1808
Goedhart S., van Rooyen R., van der Walt D. J., Maswangangye J., Sanna A., Macleod G., van den Heever S., 2019, MNRAS, 485, 4676
Guzman A., Garay G., Brooks K., Voronkov M., 2012, ApJ, 753, 51
Hosokawa T., Omukai K., 2009, ApJ, 691, 823
Hosokawa T., Yorke H. W., Omukai K., 2010, ApJ, 721, 478
Inayoshi K., Sugiyama K., Hosokawa T., Motogi K., Tanaka K. E. I., 2013, ApJ, 769, L5
Kurtz S., Franco J., 2002, Rev. Mex. AA (Serie de Conferencias), 12, 16
Kurtz S., Churchwell E., Wood D. O. S., 1994, ApJS, 91, 659
Liu T., Wu Y., Liu S.-Y., Qin S.-L., Su Y.-N., Chen H.-R., Ren Z., 2011, ApJ, 730, 17
Liu T. et al., 2017, ApJ, 849, 25
Marsh K. A., 1975, ApJ, 201, 190
Obonyo W., Lumsden S., Hoare M., Kurtz S., Purser S., 2021, MNRAS, 501, 5197
Panagia N., Felli M., 1975, A&A, 39, 1
Parfenov S. Y., Sobolev A. M., 2014, MNRAS, 444, 620
Proven-Adzri E., MacLeod G. C., van den Heever S. P., Hoare M. G., Kuditcher A., Geodhart S., 2019, MNRAS, 487, 2407
Sanna A., Menten K. M., Carreasco-Gonzalez C., Reid M. J., Ellingsen S. P., Brunthaler A., Moscadelli L., 2015, ApJ, 804, L2
Slysh V. I., Kalenskii S. V., Val'tts I. E., 2002, Astron. Rep., 46, 49
Sobolev A. M., Deguchi S., 1994a, A&A, 291, 569
Sobolev A. M., Deguchi S., 1994b, ApJ, 433, 719
Sobolev A. M., Cragg D., Ellingsen S., Gaylard M., Goedhart S., Henkel C., Voronkov M., 2007, in Chapman J. M., Baan W. A., eds, Proc. IAU Symp. 242, Astrophysical Masers and Their Environments. Cambridge Univ. Press, Cambridge, p. 81
Testi L., Hofner P., Kurtz S., Rupen M., 2000, A&A, 359, l5
van den Heever S. P., van der Walt D., Pittard J., Hoare M., 2019, MNRAS, 485, 2759
van der Walt D., 2011a, Bulletin del a Societe Royale des Science de Liège, 80, 260
van der Walt D., 2011b, AJ, 141, 152
van der Walt D., Goedhart S., Gaylard M. J., 2009, MNRAS, 398, 961
Wolf V. et al., 2024, A&A, 688, A8

This paper has been typeset from a TEX/LATEX file prepared by the author.